Nanoscale

PAPER

View Article Online
View Journal | View Issue

Cite this: *Nanoscale*, 2025, **17**, 27900

High sensitivity detection of biotinylated molecules using a high-resolution resistive pulse sensor

Heyi Chen,†[a] Jacob Brown,†[b] Ge Zhang*[b] and Jiang Zhe *[a]

Received 16th September 2025,
Accepted 18th November 2025

DOI: 10.1039/d5nr03922c

rsc.li/nanoscale

Biotinylation is a widely used technique for tagging molecules to enable their detection, isolation, or immobilization. Reliable detection of biotinylated molecules is critical for maintaining the integrity of downstream processes and ensuring the accuracy of analytical and diagnostic assays. Here, we present a novel strategy for a highly sensitive analysis of biotinylated targets based on gold nanoparticle counting. This approach integrates a high-resolution microfluidic resistive pulse sensor with a competitive nanodimer formation assay. In this method, biotinylated targets inhibit nanodimer formation between biotin- and streptavidin-modified gold nanoparticles, resulting in fewer nanodimers being produced. The change in nanodimer quantity is then measured by the resistive pulse sensor, allowing both the presence and concentration of the biotinylated target to be quantified. Using biotinylated BSA as a model target, we demonstrated that changes as small as 0.7606 pg mL^{-1} produced a significantly detectable shift in dimer ratio. Leveraging its single-particle detection capability, this strategy provides ultra-sensitive quantification with minimal calibration and sample preparation. The ability of our approach to universally detect biotinylated molecules holds great potential to advance a wide range of biotinylation applications in biotechnology, diagnostics and tissue engineering.

Introduction

Biotinylation, the covalent attachment of biotin to proteins, nucleic acids, or other molecules, is a widely used technique in molecular biology, biochemistry, and biotechnology. Biotinylated targets provide versatile tools across a broad range of biological and biomedical applications. Biotinylated proteins are commonly employed for affinity purification,[1,2] immobilization on biosensor surfaces,[3,4] or detection in assays.[5,6] Biotinylated DNA or RNA enables capture, enrichment, and detection in nucleic acid assays, including pull-downs to study protein–DNA interactions or preparation of next-generation sequencing libraries.[7–11] Biotinylated cells facilitate specific labeling,[12,13] isolation,[14,15] or tracking in flow cytometry,[16,17] imaging,[18] or adoptive transfer experiments.[19,20] Additionally, biotinylated small molecules, antibodies, or nanoparticles can be used to assemble complex molecular scaffolds,[21–23] deliver therapeutics,[24] or monitor molecular interactions[25,26] *in vitro* and *in vivo*. Detecting biotinylated molecules is critical not only to confirm successful labeling but also to quantify targets and enable downstream applications.[6,27] Without reliable and high sensitivity detection, the benefits of biotinylation, such as high specificity, strong binding, and broad applicability, cannot be fully utilized.

Several approaches are commonly employed to measure biotinylated targets, each with unique advantages and limitations. Enzyme-linked detection, including Enzyme-Linked Immunosorbent Assay (ELISA)[28] and Western blot,[29] uses streptavidin conjugated to enzymes to generate colorimetric or chemiluminescent signals, providing high sensitivity and quantitative readouts, though non-specific binding may introduce background noise.[29] Fluorescent detection leverages streptavidin-fluorophore conjugates for direct visualization *via* microscopy or flow cytometry, allowing spatial resolution[30] and multiplexing,[31] but requires careful control for photobleaching and specialized instrumentation. Affinity-based capture immobilizes biotinylated molecules on streptavidin-coated beads or surfaces for purification,[32,33] pull-downs,[5,34] or interaction studies;[35,36] while highly specific, the strong biotin–streptavidin interaction can complicate elution.[32] Mass spectrometry-based detection enables sensitive identification and quantification of multiple biotinylated targets simultaneously, though it requires extensive sample preparation and specialized equipment.[37–39] Finally, Surface-Enhanced Raman Scattering (SERS) exploits surface plasma resonances to

[a]*Department of Mechanical Engineering, University of Akron, Akron, Ohio 44325, USA. E-mail: jzhe@uakron.edu; Tel: +1-330-972-7737*
[b]*Department of Biomedical Engineering, University of Akron, Akron, Ohio 44325, USA. E-mail: gezhang@uakron.edu; Tel: +1-330-972-5237*
† These authors contributed equally as co-first authors

enhance Raman scattering signals therefore offering an ultra-high sensitivity measurement.[40,41] However, its practical use is limited by challenges such as complex optical setup and instrumentation requirements, non-specific adsorption and potential laser-induced damage to biotinylated targets.[42,43]

Resistive pulse sensors (RPSs) have been used to detect micro/nano-scale objects for decades. RPS has a simple structure yet offers unique advantages of counting single particles one by one in continuous flow. This uniqueness has enabled highly sensitive, *in situ* detection of biomolecules, including proteins,[44,45] peptides,[46,47] and DNAs.[48–51] Specifically, in combination with antigen–antibody based immunoaggregation and immunodisaggregation of microparticles, Han *et al.*[52,53] and Liu *et al.*[54] used RPSs to detect biomarkers and cell secretome. However, immunoaggregation and immunodisaggregation require well-controlled experimental conditions (*e.g.*, time, temperature, *etc.*) to eliminate nonspecific aggregation or disaggregation; the detection range of measurement is relatively narrow (*e.g.* in the range of 0.01 ng mL^{-1} to 100 ng mL^{-1} for VEGF[54]). Further, Xu *et al.* reported ultra-sensitive detection of adenosine by integrating a target-responsive aptamer-based nanoparticle release system with a high-resolution resistive pulse sensor.[55] While this method offered a wider detection range (*e.g.* 0.1 nM to 10^7 nM), it requires specific aptamer design for target biomolecules to enable the specificity of the detection. Designing aptamers that specifically recognize target molecules is time-consuming and labor-intensive, requiring careful optimization of both the aptamer's sequence and structure.

Here we present a novel gold nanoparticle-based strategy for a highly sensitive analysis of a wide variety of biotinylated targets. This approach combines a high-resolution microfluidic resistive pulse sensor with a competitive nanodimer formation assay. Using this strategy, biotinylated targets inhibit nanodimer formation between biotin- and streptavidin-modified gold nanoparticles, and the resulting changes are detected by the resistive pulse sensor. Due to its single-particle detection capability, this method achieves ultra-sensitive detection while requiring minimal calibration and sample preparation.

Materials and method

Materials

The following materials were purchased from Thermo Fisher Scientific: Dulbecco's Phosphate-Buffered Salt Solution 1× (product# MT21031CV), 400 nm Gold Nanoparticles (product# J67106.AC), and Triton X-100 non-ionic surfactant (product# AAA16046AE). The following materials were purchased from Cytodiagnostics: 200 nm Reactant Free Gold Nanoparticles (product# GRF-200-20), 150 nm Reactant Free Gold Nanoparticles (product# GRF-150-20), and 250 nm Reactant Free Gold Nanoparticles (product# GRF-250-20). The following materials were purchased from NanoPartz: Mono-Streptavidin Functionalized Spherical Gold Nanoparticle (C11-200MS-DIH-50-1), Mono-Biotin Functionalized Spherical Gold Nanoparticle (C11-200MB-DIH-50-1).

Principal

Monofunctionalized biotin gold nanoparticles (Biotin-AuNPs) and monofunctionalized streptavidin gold nanoparticles (Streptavidin-AuNPs) take advantage of biotin–streptavidin binding to form the gold nano-dimers. However, in the presence of biotinylated target biomolecules, they tend to bind with Streptavidin-AuNPs and block the binding site for Biotin-AuNPs. As a result, fewer gold nano-dimers will be formed. Hence, the percentage of nano-dimers is indicative of the amount of biotinylated target molecules present during the protein binding process. Here, we utilize a microfluidic resistive pulse sensor (RPS) to accurately count the nano-monomers (*i.e.* single Biotin-AuNPs or Streptavidin-AuNPs) and nano-dimers, from which the percentage of nano-dimers within the total count can be calculated, and the concentration of biotinylated target biomolecules can be determined.

To detect gold nano-monomer/nano-dimer *in situ* in a continuous flow, we designed a microfluidic RPS shown in Fig. 1b. The RPS sensor utilizes the Coulter counter principle.[56] An electrical field is applied across the electrolyte filled sensing channel to form an electric field and a current flow. As a gold nano-monomer/nano-dimer passes through the sensing channel, it distorts the electric field and causes a current/resistance change of the sensing channel.[57] As a result, a voltage pulse is generated, which reflects the passage of the particle. The magnitude and the pulse width of the voltage pulse are indicative of the particle's size and travel velocity.[58,59]

The microfluidic RPS device consists of a constricted sensing channel with Ag/AgCl electrodes on both sides, and an inlet/outlet reservoir on either end. The nominal dimension of the sensing channel is 2 μm (width) × 2 μm (height) × 10 μm (length). A Wheatstone bridge circuit was implemented to apply an electric field and detect the change of resistance within the sensing channel, shown in Fig. 1d. The Wheatstone bridge consists of the sensing channel itself, $R_{channel}$, two fixed resistors, R_1 and R_2, and a potentiometer, R_3. A steady DC voltage was applied at V_{in} to generate the necessary electric field. R_1 and R_2 were set to 460 kΩ to be comparable to the sensing channel's resistance (~460 kΩ) to create a balanced state of the Wheatstone bridge. R_3 was adjusted at the beginning of each test so that the voltage drop between ① and ② was zero. When a gold nano-monomer or nano-dimer passes through the sensing channel, it induces a change in the channel resistance, $R_{channel}$, which results in a voltage change between ① and ②. This voltage change is then amplified by an AD620BN differential amplifier and measured by the DAQ as V_{out}. The gain of the OP-Amp was 4491 from setting the gain resistor to be 11 Ω. The volume difference between a gold nano-monomer and a gold nano-dimer would generate a different voltage change magnitude as seen in Fig. 1c. From this difference in voltage change magnitude, the microfluidic RPS can differentiate a gold nano-monomer from a gold nano-dimer.

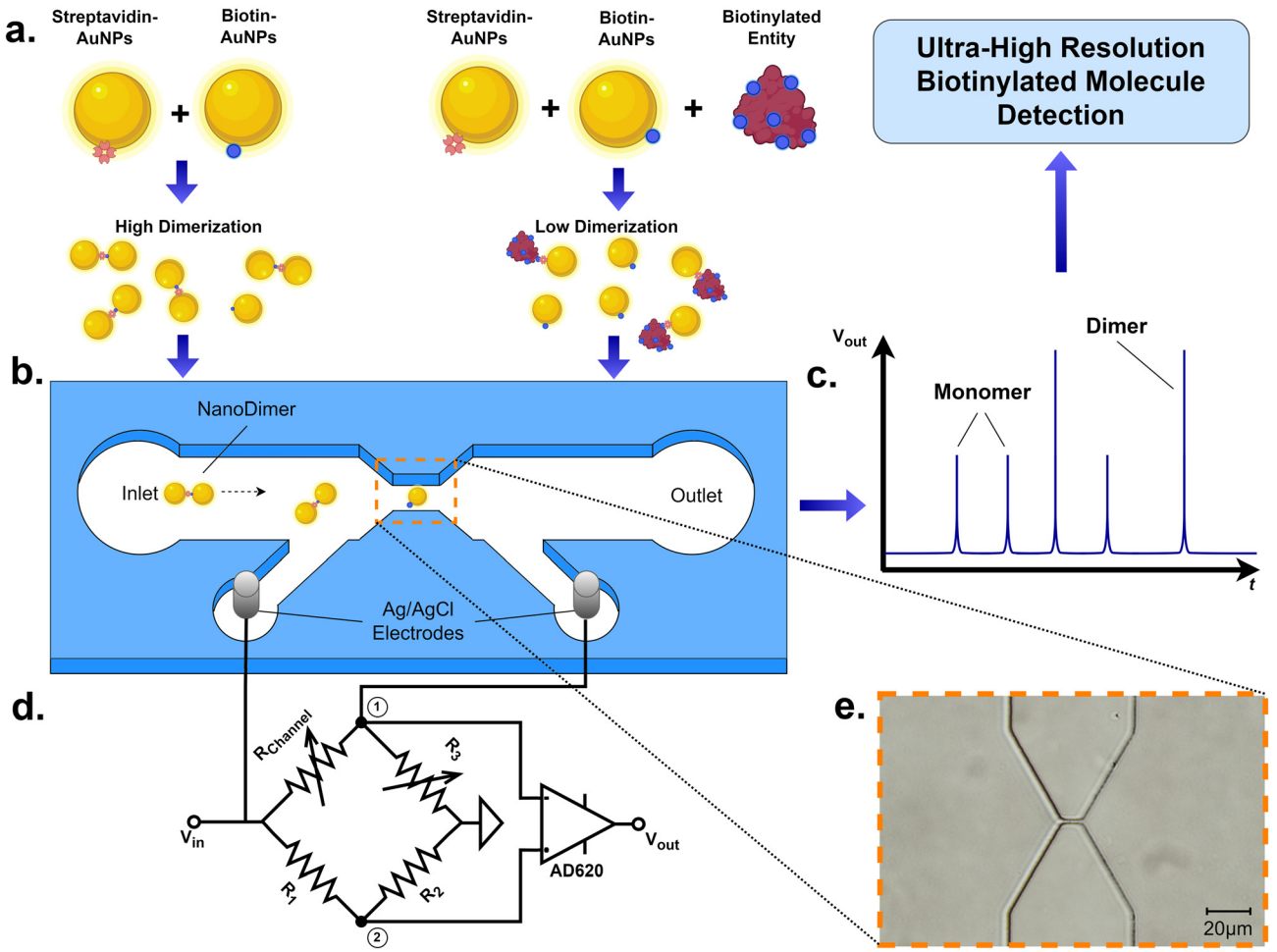

Fig. 1 (a). Molecular detection through selective tagging with streptavidin-functionalized gold nanoparticles (Streptavidin-AuNPs) and subsequent dimerization of remaining biotin-functionalized Biotin-AuNPs and Streptavidin-AuNPs. (b). Illustration of the resistive sensor for gold nano-monomer/nano-dimer measurement. (c). Illustration of the voltage pulses induced by monomers and dimers. (d). Circuit used to measure the voltage pulses. (e). Microscope image of the sensing channel in the microfluidic resistive pulse sensor on a glass substrate.

Design

Device fabrication. The microfluidic RPS was manufactured using the standard soft lithography method. The structures of the sensing channel and the reservoirs were patterned on a silicon wafer using the epoxy-based SU8-6002 negative photoresist (MicroChem, MA, USA). A 2-μm thick layer of the SU8 6002 photoresist was spin-coated on a 4-inch silicon wafer in three steps: (1) 500 rpm speed for 10 s; (2) 4000 rpm speed for 40 s; (3) 1500 rpm speed for 15 s. After spin coating, the silicon wafer was soft baked on a hot plate for 5 min at 95 °C. Next, the silicon wafer was exposed to UV radiation at 80 mJ cm^{-2}. The silicon wafer was then subjected to post exposure bake at 95 °C for 5 min. SU-8 developer is used to develop the structure pattern through a 20 s immersion, followed by an ethanol and DI water rinse. A final hard bake was implemented at 180 °C for 1 h to complete the fabrication of the micro mold. To fabricate the microchannels, the polydimethylsiloxane (PDMS, Dow Corning Sylgard 184 Silicone Elastomer Kit) was prepared and poured onto the silicon wafer in a container and then degassed. The PDMS was subsequently cured for 2 h at 65 °C. The inlet and outlet channels were punched with 1.5 mm biopsy punches; the two Ag/AgCl electrode holes were punched with a 1.0 mm biopsy punch. 1.5 mm Ag/AgCl electrodes were inserted into these holes to allow an interference fit. Finally, the PDMS slab was bonded to a glass microscope slide using air plasma treatment at 200 mTorr, 100 W, for 35 s. The dimensions of the sensing channel were measured using a surface profilometer (Dektak 150, Veeco Instrument, NY, USA). The channel measured 1.8058 ± 0.0116 μm in height, 1.5559 ± 0.0506 μm in width, and 10.8309 ± 0.1553 μm in length. Fig. 1e shows a magnified view of the sensing channel.

Nano-dimer fabrication. Nano-dimers were fabricated by conjugating mono-functionalized biotin-bound nanoparticles (Biotin-AuNPs) and monofunctionalized streptavidin-bound gold nanoparticles (Streptavidin-AuNPs). First, 200 ± 10 nm Biotin-AuNPs and Streptavidin-AuNPs in DI water (Nanopartz™) were diluted to a concentration of 2.00×10^{10} ct mL^{-1} and sonicated (Branson 2800, Branson™) separately for 30 s.

The nanoparticle suspensions were blocked by separately mixing with equal volumes of 2 wt% bovine serum albumin (BSA) aqueous solution on a shaker (Benchmark Scientific, Inc., Orbi-Shaker Jr.™) at 150 rpm for 24 hours. Next, the BSA was removed from the nanoparticle by six rounds of centrifugation for 10 minutes at 16 000*g* (Centrifuge 5415R, Eppendorf) and resuspension to 1.00×10^7 ct mL^{-1} (0.01661 pM) in ultrapure water. To conjugate Biotin-AuNPs and Streptavidin-AuNPs at different ratios, blocked nanoparticles were mixed at two separate ratios (1 : 1, 1 : 2) and incubated on a shaker (150 rpm, 24 h). To form competitively conjugated nanoparticle dimers, first, different solutions of biotin-labeled bovine albumin (bBSA) were diluted in ultrapure water. These solutions were made to have specific ratios of bBSA molecules to Biotin-AuNPs to Streptavidin-AuNPs (Biotin-AuNPs : Streptavidin-AuNPs : bBSA). For example, the 1 : 1 : 1 Biotin-AuNPs : Streptavidin-AuNPs : bBSA samples were conjugated with a 0.01661 pM bBSA solution mixed equal volumes of Biotin-AuNP and Streptavidin-AuNP suspensions, resulting in a ratio of one molecule of bBSA to each Biotin-AuNP and Streptavidin-AuNP. The Biotin-AuNPs : Streptavidin-AuNPs : bBSA solutions were mixed at different molecular ratios (0.5, 1, 2, 5, and 10) and incubated for 2 4 h, as previously described, to form competitively conjugated nano-dimers. Lastly, the conjugated nano-dimer suspensions were cleaned with the same centrifugation and resuspension steps as before and finally resuspended at a concentration of 0.50×10^9 ct ml^{-1}. To complete the sample preparation, the conjugated nano-dimer suspensions were diluted with DPBS with 0.01%v/v of Triton X-100 surfactant to $\sim 5 \times 10^7$ ct mL^{-1} for testing.

Experiment setup

For each test, air was first bled out of the microfluidic RPS with 0.2 μm filtered DPBS. Then Ag/AgCl electrodes were inserted into the electrode holes, followed by loading the sample solution into the inlet reservoir. Using a flow controller (Flow EZ, Fluigent), the pressure was kept constant at 2.5 kPa for every test. A DC voltage of 500 mV was applied across the two Ag/AgCl electrodes. The change in voltage across the Wheatstone bridge as the gold nanoparticles flow through the sensing channel was amplified by a differential amplifier (AD620BN, Analog Devices). The amplified voltage trace was recorded with a DAQ board (NI USB-6361, National Instruments) and accompanying software (LabVIEW, National Instruments) at a 500 kHz sampling rate. MATLAB was used to post-process the acquired data.

Results and discussion

Validation of RPS

To validate the high-speed nanoparticle counting capability of the RPS, reactant-free 200 nm gold nanoparticles were used. The gold nanoparticles were diluted with 1× DPBS to the desired concentrations. Once diluted, the samples were then loaded into the inlet of the device. Fig. 2a–c shows the raw voltage signals induced by the 200 nm gold nanoparticles passing through the resistive pulse sensor at three different concentrations. Within the same time frame, the higher concentration samples were seen to have induced denser voltage pulses than the lower concentration samples. Fig. 2d shows a count rate per hour at 1.44×10^7 ct mL^{-1}, 7.2×10^7 ct mL^{-1}, and 1.44×10^8 ct mL^{-1}, indicating the RPS can scan dense gold nanoparticles with high counting speed. Fig. 2e shows the peak magnitude of voltage pulses, which are tightly grouped at 0.2057 ± 0.0188 V.

To validate the RPS's capability to differentiate different-sized gold nanoparticles, reactant-free gold nanoparticles of 150 nm, 200 nm, 250 nm, and 400 nm were used. Gold nano-

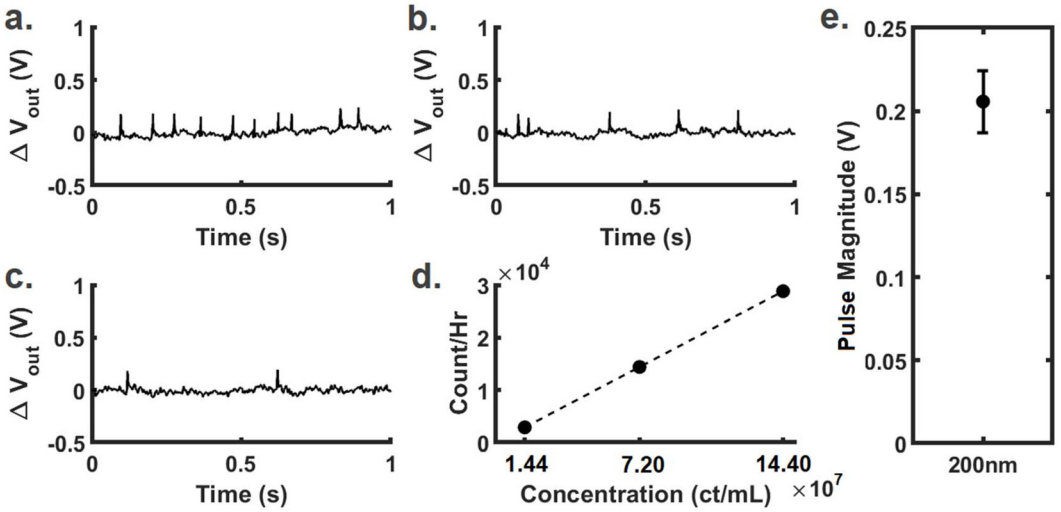

Fig. 2 Typical voltage pulses induced by 200 nm gold nanoparticles passing through the RPS. (a) At $\sim 1.44 \times 10^8$ ct mL^{-1} (b) at $\sim 7.2 \times 10^7$ ct mL^{-1} (c) at $\sim 1.44 \times 10^7$ ct mL^{-1} (d) count rate per hour at 1.44×10^7 ct mL^{-1}, 7.2×10^7 ct mL^{-1}, and 1.44×10^8 ct mL^{-1} (e) voltage pulse magnitude distribution of 200 nm gold nanoparticles.

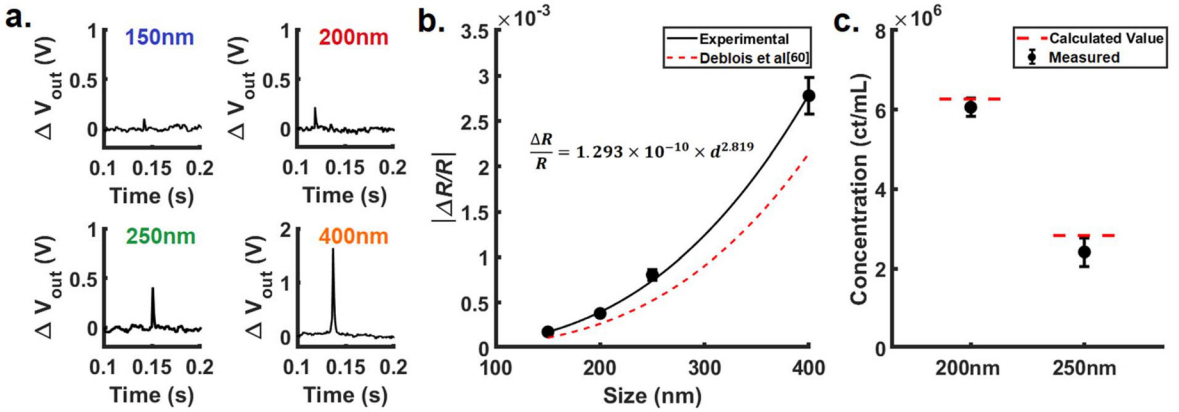

Fig. 3 Validation of the microfluidic resistive pulse device. (a) A typical voltage pulse of 150 nm, 200 nm, 250 nm, and 400 nm gold nanoparticles (note the scaling difference for the 400 nm gold nanoparticles) (b) 150 nm, 200 nm, 250 nm, and 400 nm gold nanoparticles measured $\Delta R/R$ magnitude and the theoretical $\Delta R/R$ magnitude calculated from size based on the Deblois's formula.[60] (c) Measured and calculated concentration of 200 nm and 250 nm gold nanoparticles.

particles of each size were suspended in 1× DPBS and loaded into the RPS; resistive pulses were then recorded. Fig. 3a shows typical voltage pulses by different-sized gold nanoparticles. To create the correlation curve between nanoparticle size and resistive pulse magnitude, voltage pulses ($\Delta V/V$) by 150 nm, 200 nm, 250 nm, and 400 nm were measured, which were then converted to $\Delta R/R$ with the known R_1, R_2 and R_3 values after accounting for the operational amplifier gain. Fig. 3b presents the experimental $\Delta R/R$ values *vs.* gold nanoparticle sizes. The relation is fitted with an exponential best fit correlation curve.

$$\frac{\Delta R}{R} = 1.293 \times 10^{-10} \times d^{2.819} \quad (1)$$

where d is the diameter of the gold nanoparticles in nanometers. This correlation curve clearly shows the device can distinguish/measure the sizes of different nanoparticles. It is worth noting that the $\Delta R/R$ changes induced by gold nanoparticles are distinctively larger than those predicted from Deblois's formula.[60] This echoed previous studies that found that the material composition of nanoparticles affects the resistive pulse magnitude, specifically that conductive particles generate greater RPS signal magnitude than insulating particles.[61] In short, gold nanoparticle size can be determined from the calibration curve in Fig. 3b.

To demonstrate the accuracy of the nanoparticles counting of the RPS at lower concentrations, the 200 nm and 250 nm gold nanoparticles were diluted to 6.27×10^6 ct mL^{-1} and 2.83×10^6 ct mL^{-1}, respectively (shown as the red dashed lines in Fig. 3a). Each sample was then loaded into the RPS. Voltage pulse traces were recorded. The measurement was run 5 times in the RPS with a 1× DPBS flushing in between each run.

To obtain the concentration values shown in Fig. 3c, we first obtained the flow rate 'f' at the microchannel based on the set pressure, channel dimensions, viscosity, and density of the DPBS. Second, the total fluid volume 'v' through the sensing channel within a time period 't' was calculated by $v = f \cdot t$. Lastly, the number of voltage pulses 'n' within the period 't' was then measured; each pulse represents one gold nanoparticle passing the sensing channel. The concentration was obtained as n/v. As shown in Fig. 3c, the 200 nm and 250 nm gold nanoparticles concentrations were measured to be $6.062 \times 10^6 \pm 0.225 \times 10^6$ ct mL^{-1} and $2.414 \times 10^6 \pm 0.352 \times 10^6$ ct mL^{-1}, respectively, which matched well with the nominal concentration. The small difference could possibly be caused by the settlement of a small number of gold nanoparticles on the channel substrate.

We selected AuNP concentrations ranging from 2.83×10^6 ct mL^{-1} to 1.44×10^8 ct mL^{-1}, so that it would be rare that two AuNPs would enter the sensing channel at the exact same time. In the event that multiple nanoparticles are present in the sensing channel at different moments, the voltage pulse would exhibit a stepped pyramid structure, from which the individual AuNPs can be identified.

Validation of the formation of nano-dimers

Monofunctionalized biotin gold nanoparticles (Biotin-AuNPs) and monofunctionalized gold nanoparticles (Streptavidin-AuNPs) were taken from their original packaging. Nominal sizes of these gold nanoparticles are 200 ± 25 nm. Both Biotin-AuNPs and Streptavidin-AuNPs suspensions were diluted to 1.0×10^7 np mL^{-1} (0.01661 pM), and the suspensions were blocked with 100 μL of 2% BSA and incubated on a shaker at 150 rpm for 24 h. Blocked gold nanoparticles were washed six times by centrifugation at 16 000*g*, 5 min. To conjugate Biotin-AuNPs and Streptavidin-AuNPs to different ratios of nano-dimers, blocked gold nanoparticles were mixed at various ratios (1 : 1, 1 : 2) and incubated on a shaker (150 rpm, 24 h). To form competitively conjugated nano-dimers, an equal number of blocked, functionalized gold nanoparticles were mixed with biotin-labeled bovine albumin (bBSA) at different molar ratios. All conjugated gold nanoparticles were washed

six times by centrifugation (16 000*g*, 5 min) and resuspended in 100 μL for testing.

To validate the formation of the nano-dimers through biotin–streptavidin binding, we used the microfluidic RPS to measure the nano-dimers formed through the resistive pulse magnitude. This measurement also creates a baseline to be referenced in later tests where biotinylated BSA was used to alter the dimerization ratios through competitive binding with Biotin-AuNPs. The Biotin-AuNPs and the Streptavidin-AuNPs were mixed at a 1 : 1 and 1 : 2 ratio. The samples were loaded separately into the microfluidic device, and the voltage pulses ($\Delta V/V$) induced by the gold nano-monomers and gold nano-dimers were recorded and converted to $\Delta R/R$. As the volume of the Biotin-AuNP or Streptavidin-AuNP nano-monomer is $\frac{1}{2}$ of the size of the formed nano-dimers, the resistive pulse sensor had distinctive resistive pulses as shown in Fig. 4a. The sizes of Biotin-AuNPs and Streptavidin-AuNPs were calculated from the correlation curve shown in Fig. 3b, 199.8565 ± 15.2850 nm, which matched with the nominal size, 200 nm ± 10 nm well. Similarly, from the pulses generated by the nano-dimers. We calculate the equivalent dimeter of the nano-dimers to be 254.1566 ± 13.6963 nm, which is in good agreement of its equivalent diameter (*i.e.* $\sqrt[3]{2 \times 200^3} = 252$ nm). From the measured voltage pulses we can identify nano-dimers from nano-monomers and count them accurately *via* pulse magnitude. From these counts with a ~30-minute time frame, the nano-dimer ratio was calculated. 6 sample sets were measured for each mixing ratio. Fig. 4b shows the measurement results. Measurements show 45.612 ± 4.389% dimer ratio when mixing Biotin-AuNPs : Streptavidin-AuNPs mixing ratio was 1 : 1. The nano-dimer ratio dropped to 29.706 ± 3.675% when the Biotin-AuNPs : Streptavidin-AuNPs mixing ratio was changed to 1 : 2. The change in nano-dimer ratios was also visually confirmed with TEM imaging seen in Fig. 4c. The measured nano-dimer ratios were consistent with the theoretical calculations (red dashed lines in Fig. 4b).

Per the specification sheet from NanoPartz, the manufacturer of the Streptavidin-AuNPs and Biotin-AuNPs, these NPs have a ~70% functionalization ratio. At a 1 : 1 Biotin-AuNP : Streptavidin-AuNP mixing ratio, assuming that 70 out of 100 of the functionalized Biotin-AuNPs and Streptavidin-AuNPs bond with each other to form nano-dimers, 70 nano-dimers would be formed, with the remaining unfunctionalized Biotin-AuNPs and Streptavidin-AuNPs leaving behind 30 nano-monomers each. This would create a total of 130 nanoparticles (70 nano-dimers and 60 nano-monomers), yielding a theoretical maximum of 53.8% nano-dimer ratio *via* streptavidin-biotin binding (shown as the red dashed line in Fig. 4b). A change in the Biotin-AuNP : Streptavidin-AuNP mixing ratio would change the ratio of nano-dimers due to a change in available protein for binding. At a 1 : 2 Biotin-AuNP : Streptavidin-AuNP ratio, the theoretical nano-dimer ratio was estimated to be 30.4%. Compared to the theoretical predictions, the measured nano-dimer ratio at 1 : 2 Biotin-AuNP : Streptavidin-AuNP matched very well with the theoretical prediction. At 1 : 1 Biotin-AuNP : Streptavidin-AuNP, the measured nano-dimer ratio was 45.6%, which is 18% lower than the maximum prediction (53.8%). Note that the predicted maximum nano-dimer ratio is an ideal value that is difficult to obtain due to functionalization variances in the Biotin-AuNPs and Streptavidin-AuNPs, which is common in mono-functionalization of gold nanoparticles.[62,63] Nevertheless, the nano-dimer ratios at 1 : 1 Biotin-AuNP : Streptavidin-AuNP were higher because more binding site pairs were available.

Testing of biotinylated molecules

Next, to simulate the biotinylated molecule detection, biotinylated BSA (bBSA), was used as a model target molecule to compete against Biotin-AuNPs in protein binding with the Streptavidin-AuNPs. In principle, by introducing the bBSA at increasing ratios, the number of free Streptavidin-AuNPs available for dimerization with Biotin-AuNPs decreases. By correlating the dimer ratio with Biotin-AuNP : Streptavidin-AuNP : bBSA ratios, the number of biotinylated molecules can be estimated.

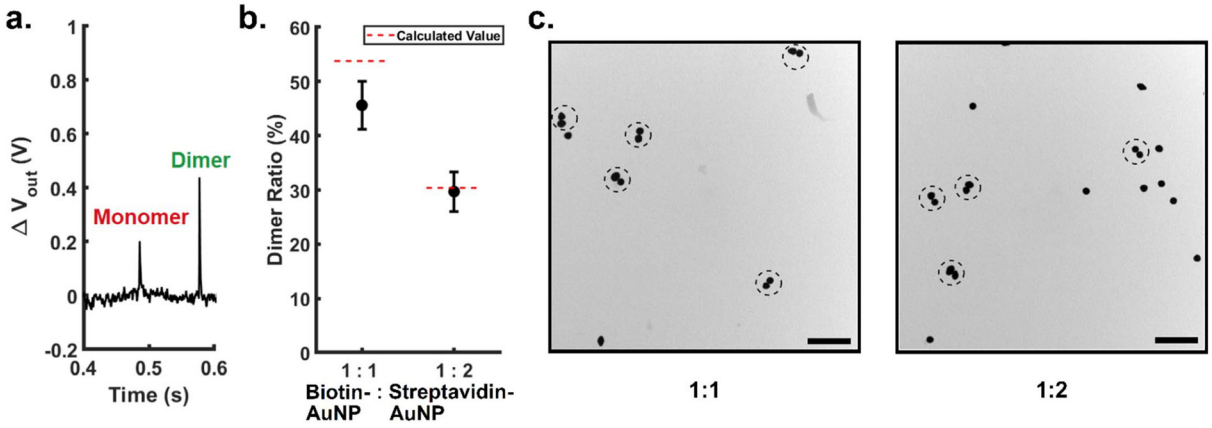

Fig. 4 (a) Typical voltage pulses by a nano-monomer and a nano-dimer. (b) Nano-dimer ratio of Biotin-AuNP : Streptavidin-AuNP at 1 : 1 and 1 : 2 mixing ratio. (c) TEM Images of Biotin-AuNP : Streptavidin-AuNP at 1 : 1 ratio and 1 : 2 ratio. (The scale bar represents 1.0 μm.)

We used the microfluidic device to measure the nano-dimer ratio of the following Biotin-AuNP : Streptavidin-AuNP : bBSA mixing ratios: 1 : 1 : 0, 1 : 1 : 0.5, 1 : 1 : 1, 1 : 1 : 2, 1 : 1 : 5, and 1 : 1 : 10. The results are shown in Fig. 5. Note that the nano-dimer ratio of MB : MS mixing ratio of 1 : 1 previously measured in Fig. 3 (with no bBSA) is labeled here as 1 : 1 : 0. The total NP concentration was maintained at ~1 × 10^7 ct mL^{-1} during dimer conjugation. The bBSA solutions based on molecular ratios were made by serial dilutions to ensure the Biotin-AuNP : Streptavidin-AuNP : bBSA ratio during dimer conjugation. A Student's *T*-test was also performed to establish the significance of the difference between each Biotin-AuNP : Streptavidin-AuNP : bBSA mixing ratios.

Fig. 5 indicates that the nano-dimer ratios decreased with increasing the bBSA ratio. TEM images of the Biotin-AuNP : Streptavidin-AuNP : bBSA mixing ratios were presented in Fig. 5 to validate the measured tendency. This tendency closely resembled a one-phase exponential decay, an expected result in competitive binding assays, where bBSA acts as a binding inhibitor and the dimerization percentage acts as the signal. In competitive binding assays, the signal is indirectly proportional to the concentration of the analyte and the relationship between the signal and analyte concentration can be defined using a one-phase exponential decay as a calibration curve.[64] Using nonlinear regression, we fit a one-phase exponential decay curve to the measured dimer ratios as a function of bBSA ratio in Fig. 5. A R^2 value of 0.9765 was obtained.

At a Biotin-AuNP : Streptavidin-AuNP : bBSA mixing ratio of 1 : 1 : 0.5, the nanoparticles had a concentration of 0.01661 pM, and the bBSA concentration was 0.00831 pM. According to the bBSA certificate of analysis, the molar mass of the bBSA is 68 629 g mol^{-1}, resulting in 0.5 parts being equivalent to 0.570 pg mL^{-1} in our tests. A Student's *T*-test shows a *p*-value of

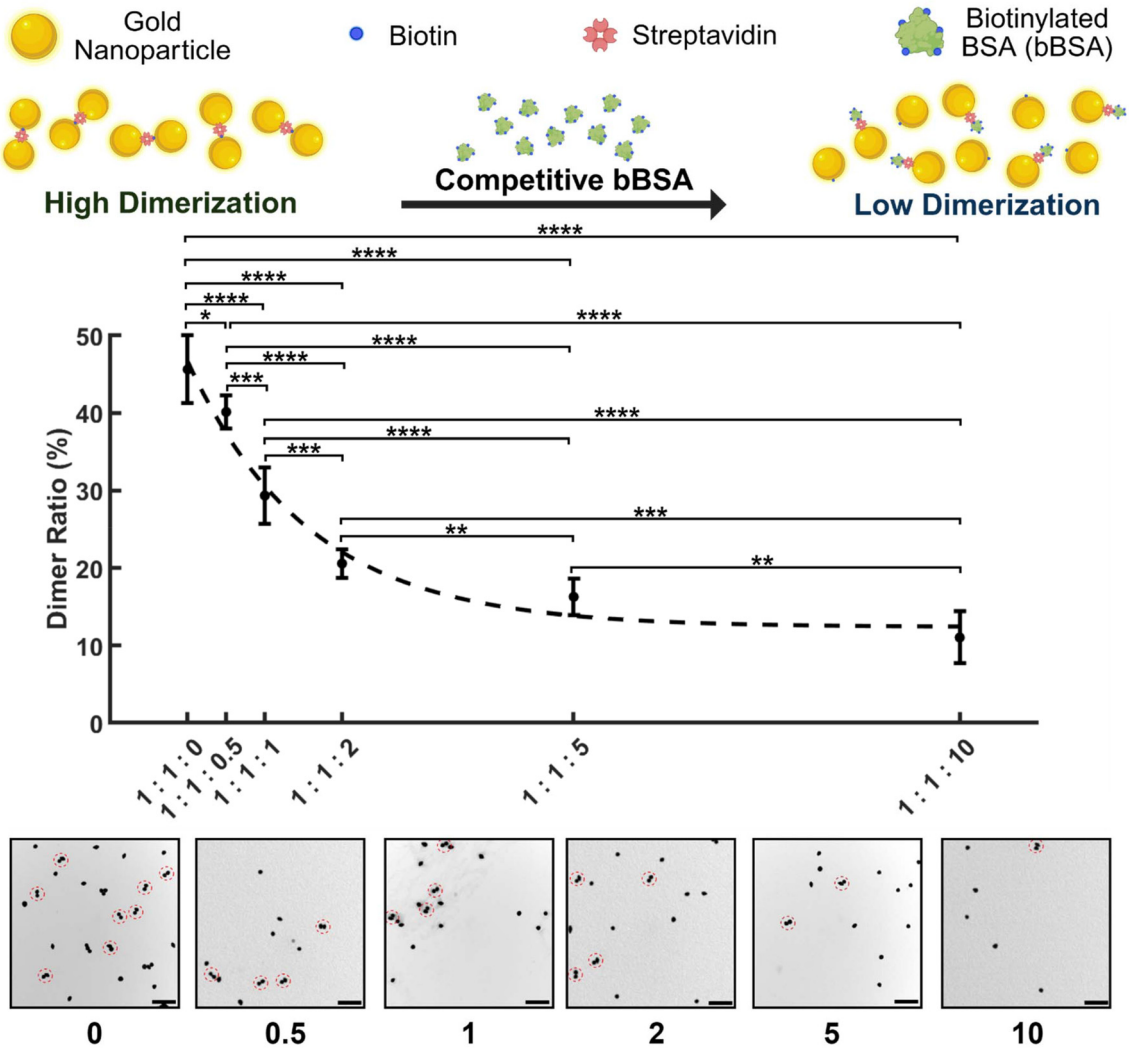

Fig. 5 The measured dimer concentration at different Biotin-AuNPs, Streptavidin-AuNPs and biotinylated BSA mixing ratios (Biotin-AuNP : Streptavidin-AuNP : bBSA) and accompanying TEM images. (The scale bar represents 1.0 μm.) Each error bar represents the standard deviation of 6 tests.

0.0142 between the ratios of 1 : 1 : 0 and 1 : 1 : 0.5, demonstrating the microfluidic device's ability to detect a minimum concentration of 0.570 pg mL^{-1}. As bBSA increases by another 0.5 parts, a *p*-value of 0.0001315 was shown between 1 : 1 : 0.5 and 1 : 1 : 1. Note that a similar sample matrix and calibration approach were used in our method to derive the LoD and LoQ for comparison with ELISA or magneto-ELISA. From Fig. 5, we used equations given by Armbruster *et al.* and Taleuzzaman *et al.* that extrapolated on Clinical and Laboratory Standards Institute (CLSI) EP17 guideline for LoD and LoQ.[65,66] Details of the formula and the calculations are provided in SI. The LoD and LoQ were calculated to be 0.7606 pg mL^{-1} and 2.3044 pg mL^{-1} respectively. In comparison, commercially available Biotin detection ELISA kits such as IDK® Biotin ELISA and Biotin Quantitative Determination ELISA typically have higher LoD and LoQ values.[67,68] IDK® Biotin ELISA reported a LoD of 32.4 pg mL^{-1} and LoQ of 41.8 pg mL^{-1},[67] while Biotin Quantitative Determination ELISA reported a LoD of 190 pg mL^{-1} and LoQ of ~310 pg mL^{-1}.[68] More advanced ELISA, such as magneto-ELISA reports a LoD as low as 2 pg mL^{-1}.[69] Our method shows significantly lower LoD and LoQ and a significant improvement in sensitivity against existing methods.

Fig. 5 presents a standard curve for biotinylated biomolecules. A detectable difference in values indicates that our method can quantify the concentration of bBSA in the range of 0.5 parts to 10 parts or 0.570 pg mL^{-1} to 11.4 pg mL^{-1}. It can be inferred that when the mixing ratios of Biotin-AuNP : Streptavidin-AuNP : biotinylated biomolecules are maintained, the nano-dimer ratio would follow a similar trend shown in Fig. 5. Based on binding kinetics, the proportion of streptavidin binding sites occupied by biotinylated biomolecules *vs.* Biotin-AuNPs is only dictated by changes in relative concentration and the complex formation and dissociation constants, properties inherent to the biotin–streptavidin complex.[70] This suggests that this system could be used with a wide range of concentrations of biotinylated molecules. Due to the single entity detection of our technique paired with our utilization of enzyme kinetics, in principle, our system has the capability to measure biomolecules at even much lower concentrations. Note here that while measurement uncertainty in dimer ratio exists among samples, it has minimum effect on the overall relationship between biotinylated molecules ratio and dimer ratio. The statistics analysis showed that there existed distinctive differences in dimer ratios as bBSA were added at all concentrations (see Fig. 5).

We also conducted a negative control test using VEGF protein with a high concentration (1 : 1 : 4076 Biotin-AuNP : Streptavidin-AuNP : VEGF). The details and results are provided in SI. A *T*-test suggests that the presence of VEGF protein did not affect the biotin–streptavidin binding, nor did it affect the dimer ratio and thus the biotinylated biomolecule detection.

BSA has high structural similarity to human serum albumin (HSA),[71,72] which comprises about 60% of plasma proteins, making it one of the most common proteins in the human body.[73,74] Additionally, BSA is one of the most thoroughly studied, consistently produced, and stable proteins, widely used as a reliable standard and blocking agent for biomolecular assays.[73,75] While bBSA was used to demonstrate the detection of biotinylated biomolecules, this method would work for other biotinylated biomolecules. Biotin–streptavidin binding has an extremely high binding affinity that is largely unaffected by interactions with its target ligand.[76] As examples, biotinylated antibodies, antigens, DNA/RNA, lipids and hormones have all been used in numerous detection-based applications ranging from diagnostic immunoassays, diagnostics and drug delivery that can also compete against Biotin-AuNPs in protein binding with the Streptavidin-AuNPs and change the nano-dimer ratio.

In this study, biotinylated BSA (bBSA) was used as a model target to validate our approach. Our strategy relies on the biotin–streptavidin interaction, which has exceptionally high binding affinity and is widely applicable across various biotinylated biomolecules. For instance, biotinylated antibodies, antigens, nucleic acids, lipids, and hormones have all been successfully employed in biotin–streptavidin-based detection platforms for diagnostics, biosensing, and drug delivery. In principle, our device should therefore be compatible with a broad range of biotinylated species, as they can compete with Biotin-AuNPs for streptavidin binding and alter the nano-dimer ratio, which is the basis of our detection mechanism. However, the detection sensitivity, specificity, and kinetics may vary depending on the molecular size and biotin valency of the target. Larger biomolecules may impose steric hindrance, slowing the binding rate and reducing effective affinity, thereby impacting sensitivity and response time. Additionally, biotin valency can influence interaction strength. Higher valency enhances binding sensitivity but may compromise specificity due to increased risk of nonspecific aggregation. These factors will be systematically evaluated in future studies to further optimize the performance of our device across diverse biotinylated targets.

Biotin interference is a potential limitation of our device when applied directly to clinical samples, as free biotin may compete with the biotinylated target for streptavidin binding and reduce detection accuracy. Therefore, clinical samples would need to be pretreated to remove or reduce free biotin prior to testing. Additionally, spike-recovery experiments should be conducted to verify assay robustness and quantify any bias introduced by residual free biotin before clinical implementation.

In our tests, the total turnaround time of the assay time was 25 hours from preparing the sample to subsequent testing, while the incubation time is 24 hours. Literature suggest that utilizing similar binding techniques and conditions, other nanoparticle-based systems were conjugated in as little as 30 min at room temperature.[77,78] Factors such as agitation speed, temperature, and analyte concentration likely impact the adequate incubation time. In comparison, depending on the type of assay, incubation time of traditional ELISA varies between 4.5-hours to overnight.[79–81] Additional time is required for repeating washing steps and absorbance reading. With the demonstration of the new assay method based on

RPS sensing technology, we plan to optimize the conditions to significantly reduce the incubation time in our future work. Due to the small dimensions of the sensing channel, the device can only analyze a small sample volume and has limited throughput. However, the throughput can be improved using parallel sensing channels in combination with signal multiplexing strategies.[82,83]

During our test, we found small amounts of protein (*e.g.* biotin, streptavidin) adhered to the channel surface and they attended to adhere to each other and form large protein clusters, which would cause measurement uncertainty. In our tests, we intentionally reduced the Streptavidin-AuNP : Biotin-AuNP concentration to 5×10^7 ct mL^{-1} to reduce the post aggregation of protein. Triton X-100, a non-ionic surfactant, was used to treat the channel surface, which seemed to have reduced protein adhesion and post aggregation. Recently, Pluronic F-127 was reported to have successfully reduced protein adhesion to PDMS surface.[84] This coating can be potentially applied to our device to further reduce the protein adhesion.

Conclusions

We present a novel method based on gold nanoparticle counting for a highly sensitive analysis of biotinylated targets. This method combines a high-resolution microfluidic resistive pulse sensor with a competitive nano-dimer formation assay. As biotinylated molecules inhibit nano-dimer formation between biotin- and streptavidin-modified gold nanoparticles, the concentration of the target biotinylated molecules can be determined by counting the ratio of nano-dimers. The nanoparticle counting was conducted through resistive pulse measurement with bBSA acting as the target biotinylated molecule. Results showed that a change in bBSA as small as 0.7606 pg mL^{-1} can create a statistically significant difference in nano-dimer ratio. With the single nanoparticle detection resolution, this method offers ultra-high sensitivity with minimal calibration and sample preparation. Additionally, bBSA concentration ratio *vs.* dimer ratio closely resembles a one phase exponential decay. Other biotinylated molecules are expected to follow this trend. Hence this method can be used to detect and quantification of a variety of biotinylated biomolecules with similar sensitivity and shows great potential for numerous fields in biology and biotechnology including molecular biology, biochemistry, diagnostics and clinical research, and tissue engineering.

Author contributions

Heyi Chen, Ge Zhang and Jiang Zhe drafted the manuscript. Chen and Brown contributed equally to device fabrication, sample preparation, testing and data analysis. Jiang Zhe and Ge Zhang acquired the funding, formulated the research goals, and directed the project equally.

Conflicts of interest

There are no conflicts to declare.

Data availability

The processed data supporting this article is available in The University of Akron OneDrive Folder "AuNPs Data" folder at AuNPs Data.

The supplementary information includes details of 1) LOD and LOQ calculations, and 2) Negative control test with non-biotinylated protein. See DOI: https://doi.org/10.1039/d5nr03922c.

Acknowledgements

This work was supported by the National Science Foundation of USA under award numbers ECCS 2232940. Any opinions, findings, and conclusions or recommendations expressed in this material are those of the author(s) and do not necessarily reflect the views of the National Science Foundation.

References

1 K. J. Schreiber, E. Kadijk and J.-Y. Youn, *J. Proteome Res.*, 2024, **23**, 1531–1543.
2 R. E. Kattan, D. Ayesh and W. Wang, *Briefings Bioinf.*, 2023, **24**, bbad010.
3 K. Sari, Y. W. Hartati and S. Gaffar, *Anal. Bioanal. Electrochem.*, 2022, **14**, 127–143.
4 E. Beitello, K. Osei, T. Kobulnicky, F. Breausche, J. A. Friesen and J. D. Driskell, *Langmuir*, 2025, **41**, 10576–10585.
5 Y. Tabana, D. Babu, R. Fahlman, A. G. Siraki and K. Barakat, *BMC Biotechnol.*, 2023, **23**, 44.
6 H. A. Balzer and C. B. Whitehurst, *Curr. Issues Mol. Biol.*, 2023, **45**, 8733–8754.
7 F. Cozzolino, I. Iacobucci, V. Monaco and M. Monti, *J. Proteome Res.*, 2021, **20**, 3018–3030.
8 M. M. Makowski, C. Gräwe, B. M. Foster, N. V. Nguyen, T. Bartke and M. Vermeulen, *Nat. Commun.*, 2018, **9**, 1653.
9 J. Engreitz, E. S. Lander and M. Guttman, in *Nuclear Bodies and Noncoding RNAs: Methods and Protocols*, ed. S. Nakagawa and T. Hirose, Springer, New York, NY, 2015, pp. 183–197. ISBN: 978-1-4939-2253-6.
10 Y. Wang, Y. Xiao, S. Dong, Q. Yu and G. Jia, *Nat. Chem. Biol.*, 2020, **16**, 896–903.
11 K. Hartstock, B. S. Nilges, A. Ovcharenko, N. V. Cornelissen, N. Püllen, A.-M. Lawrence-Dörner, S. A. Leidel and A. Rentmeister, *Angew. Chem., Int. Ed.*, 2018, **57**, 6342–6346.
12 S. Rayaprolu, S. Bitarafan, J. V. Santiago, R. Betarbet, S. Sunna, L. Cheng, H. Xiao, R. S. Nelson, P. Kumar, P. Bagchi, D. M. Duong, A. M. Goettemoeller, V. J. Oláh,

M. Rowan, A. I. Levey, L. B. Wood, N. T. Seyfried and S. Rangaraju, *Nat. Commun.*, 2022, **13**, 2927.
13 H. Liu, H. Luo, Q. Xue, S. Qin, S. Qiu, S. Liu, J. Lin, J. P. Li and P. R. Chen, *J. Am. Chem. Soc.*, 2022, **144**, 5517–5526.
14 S. Ayaz-Guner, M. B. Acar, D. Boyvat, H. Guner, H. Bozalan, M. Güzel, S. K. Yıldır, N. Altınsoy, F. Fındık, M. Karakükçü and S. Özcan, *STAR Protoc.*, 2022, **3**, 101863.
15 H.-J. Jou, L.-Y. Chou, W.-C. Chang, H.-C. Ho, W.-T. Zhang, P.-Y. Ling, K.-H. Tsai, S.-H. Chen, T.-H. Chen, P.-H. Lo, M. Chen and H.-T. Hsu, *Micromachines*, 2021, **12**, 473.
16 M. Ayer, O. Burri, R. Guiet, A. Seitz, E. Kaba, B. Engelhardt and H.-A. Klok, *Bioconjugate Chem.*, 2021, **32**, 541–552.
17 C. Ravanat, A. Pongérard, M. Freund, V. Heim, F. Rudwill, C. Ziessel, A. Eckly, F. Proamer, H. Isola and C. Gachet, *Transfusion*, 2021, **61**, 1642–1653.
18 A. Bera, A. Nepalia, A. Upadhyay, D. K. Saini and A. R. Chakravarty, *Dalton Trans.*, 2023, **52**, 13339–13350.
19 D. Pan, Y. Wang, N. Xu, Y. Xu, X. Wang, L. Wang, J. Yan, L. Yu, L. Miao, G. Wang and M. Yang, *Eur. J. Nucl. Med. Mol. Imaging*, 2022, **49**, 4419–4426.
20 G. Pasqual, A. Chudnovskiy and G. D. Victora, in *Dendritic Cells: Methods and Protocols*, ed. V. Sisirak, Springer US, New York, NY, 2023, pp. 71–80. ISBN: 978-1-0716-2938-3.
21 D. Sato, Z. Wu, H. Fujita and J. S. Lindsey, *Organics*, 2021, **2**, 161–273.
22 S. Brannetti, S. Gentile, A. Chamorro-Garcia, L. Barbero, E. Del Grosso and F. Ricci, *Angew. Chem.*, 2023, **135**, e202313243.
23 W. Li, S. Yin, Y. Shen, H. Li, L. Yuan and X.-B. Zhang, *J. Am. Chem. Soc.*, 2023, **145**, 3736–3747.
24 C. Wang, Y. Xiu, Y. Zhang, Y. Wang, J. Xu, W. Yu and D. Xing, *Nanoscale*, 2025, **17**, 1812–1873.
25 X. Fei, S. Kwon, J. Jang, M. Seo, S. Yu, T. W. Corson and S.-Y. Seo, *Biomolecules*, 2024, **14**, 785.
26 X. Lin, M. A. S. Fonseca, J. J. Breunig, R. I. Corona and K. Lawrenson, *RNA Biol.*, 2021, **18**, 2203–2217.
27 E. Oquendo, J. Savoie, J. M. Swenson and C. Grimaldi, *Bioanalysis*, 2021, **13**, 847–860.
28 H. Hayrapetyan, T. Tran, E. Tellez-Corrales and C. Madiraju, in *ELISA: Methods and Protocols*, ed. R. S. Matson, Springer US, New York, NY, 2023, vol. 2612, pp. 1–17.
29 R. Sule, G. Rivera and A. V. Gomes, *BioTechniques*, 2023, **75**, 99–114.
30 G. Kumar, R. K. Pandurengan, E. R. Parra, K. Kannan and C. Haymaker, *Front. Immunol.*, 2023, **14**, 1288802.
31 C. Laberiano-Fernández, S. Hernández-Ruiz, F. Rojas and E. R. Parra, *Front. Mol. Biosci.*, 2021, **8**, 660202.
32 A. S. Pina, Í. L. Batalha, A. M. G. C. Dias and A. C. A. Roque, in *Protein Downstream Processing: Design, Development, and Application of High and Low-Resolution Methods*, ed. N. E. Labrou, Springer US, New York, NY, 2021, pp. 107–132. ISBN: 978-1-62703-976-5.
33 T. G. M. Schmidt, L. Batz, L. Bonet, U. Carl, G. Holzapfel, K. Kiem, K. Matulewicz, D. Niermeier, I. Schuchardt and K. Stanar, *Protein Expression Purif.*, 2013, **92**, 54–61.
34 J. Kimmel, J. Kehrer, F. Frischknecht and T. Spielmann, *Mol. Microbiol.*, 2022, **117**, 553–568.
35 K. K. Lum and I. M. Cristea, *Expert Rev. Proteomics*, 2016, **13**, 325–340.
36 T. C. Branon, J. A. Bosch, A. D. Sanchez, N. D. Udeshi, T. Svinkina, S. A. Carr, J. L. Feldman, N. Perrimon and A. Y. Ting, *Nat. Biotechnol.*, 2018, **36**, 880–887.
37 L. V. DeSouza and K. W. M. Siu, *Clin. Biochem.*, 2013, **46**, 421–431.
38 R. Terracciano, M. Preianò, A. Fregola, C. Pelaia, T. Montalcini and R. Savino, *Int. J. Mol. Sci.*, 2021, **22**, 532.
39 W. van Bergen, A. J. R. Heck and M. P. Baggelaar, *Curr. Opin. Chem. Biol.*, 2022, **66**, 102074.
40 G. McNay, D. Eustace, W. E. Smith, K. Faulds and D. Graham, *Appl. Spectrosc.*, 2011, **65**, 825–837.
41 S. E. J. Bell, G. Charron, E. Cortés, J. Kneipp, M. L. de la Chapelle, J. Langer, M. Procházka, V. Tran and S. Schlücker, *Angew. Chem., Int. Ed.*, 2020, **59**, 5454–5462.
42 K. Eberhardt, C. Stiebing, C. Matthäus, M. Schmitt and J. Popp, *Expert Rev. Mol. Diagn.*, 2015, **15**, 773–787.
43 J. Langer, D. Jimenez de Aberasturi, J. Aizpurua, R. A. Alvarez-Puebla, B. Auguié, J. J. Baumberg, G. C. Bazan, S. E. J. Bell, A. Boisen, A. G. Brolo, J. Choo, D. Cialla-May, V. Deckert, L. Fabris, K. Faulds, F. J. García de Abajo, R. Goodacre, D. Graham, A. J. Haes, C. L. Haynes, C. Huck, T. Itoh, M. Käll, J. Kneipp, N. A. Kotov, H. Kuang, E. C. Le Ru, H. K. Lee, J.-F. Li, X. Y. Ling, S. A. Maier, T. Mayerhöfer, M. Moskovits, K. Murakoshi, J.-M. Nam, S. Nie, Y. Ozaki, I. Pastoriza-Santos, J. Perez-Juste, J. Popp, A. Pucci, S. Reich, B. Ren, G. C. Schatz, T. Shegai, S. Schlücker, L.-L. Tay, K. G. Thomas, Z.-Q. Tian, R. P. Van Duyne, T. Vo-Dinh, Y. Wang, K. A. Willets, C. Xu, H. Xu, Y. Xu, Y. S. Yamamoto, B. Zhao and L. M. Liz-Marzán, *ACS Nano*, 2020, 14, 28–117.
44 L. T. Sexton, L. P. Horne, S. A. Sherrill, G. W. Bishop, L. A. Baker and C. R. Martin, *J. Am. Chem. Soc.*, 2007, **129**, 13144–13152.
45 J. Sha, T. Hasan, S. Milana, C. Bertulli, N. A. W. Bell, G. Privitera, Z. Ni, Y. Chen, F. Bonaccorso, A. C. Ferrari, U. F. Keyser and Y. Y. S. Huang, *ACS Nano*, 2013, **7**, 8857–8869.
46 I. Heaton and M. Platt, *Anal. Chem.*, 2019, **91**, 11291–11296.
47 R. Maugi, Z. Salkenova and M. Platt, *Med. Devices Sens.*, 2020, **3**, e10059.
48 A. Arima, M. Tsutsui, I. H. Harlisa, T. Yoshida, M. Tanaka, K. Yokota, W. Tonomura, M. Taniguchi, M. Okochi, T. Washio and T. Kawai, *Sci. Rep.*, 2018, **8**, 16305.
49 C. C. Harrell, Y. Choi, L. P. Horne, L. A. Baker, Z. S. Siwy and C. R. Martin, *Langmuir*, 2006, **22**, 10837–10843.
50 L. Yang and T. Yamamoto, *Front. Microbiol.*, 2016, **7**, 1500.
51 K. Zhou, L. Li, Z. Tan, A. Zlotnick and S. C. Jacobson, *J. Am. Chem. Soc.*, 2011, **133**, 1618–1621.
52 Y. Han, H. Wu, F. Liu, G. Cheng and J. Zhe, *Anal. Chem.*, 2014, **86**, 9717–9722.
53 Y. Han, H. Wu, F. Liu, G. Cheng and J. Zhe, *Biomicrofluidics*, 2016, **10**, 024109.

54 F. Liu, P. Kc, L. Ni, G. Zhang and J. Zhe, *Organogenesis*, 2018, **14**, 67–81.
55 R. Xu, L. Abune, B. Davis, L. Ouyang, G. Zhang, Y. Wang and J. Zhe, *Biosens. Bioelectron.*, 2022, **203**, 114023.
56 G. M. Don, *JALA*, 2003, **8**, 72–81.
57 Y. Song, J. Zhang and D. Li, *Micromachines*, 2017, **8**, 204.
58 R. W. DeBlois and R. K. Wesley, *J. Virol.*, 1977, **23**, 227–233.
59 P. Hinkle, T. M. Westerhof, Y. Qiu, D. J. Mallin, M. L. Wallace, E. L. Nelson, P. Taborek and Z. S. Siwy, *Sci. Rep.*, 2017, **7**, 10173.
60 R. W. DeBlois and C. P. Bean, *Rev. Sci. Instrum.*, 1970, **41**, 909–916.
61 Y. Song, C. Wang, R. Sun, X. Pan and D. Li, *J. Colloid Interface Sci.*, 2014, **423**, 20–24.
62 Q. Huo and J. G. Worden, *J. Nanopart. Res.*, 2006, **9**, 1013–1025.
63 K.-M. Sung, D. W. Mosley, B. R. Peelle, S. Zhang and J. M. Jacobson, *J. Am. Chem. Soc.*, 2004, **126**, 5064–5065.
64 D. Wild, in *The Immunoassay Handbook*, Elsevier, 2013, pp. 7–10. ISBN: 978-0-08-097037-0.
65 D. A. Armbruster and T. Pry, *Clin. Biochem. Rev.*, 2008, **29**, S49–S52.
66 M. Taleuzzaman, *Org. Med. Chem. Int. J.*, 2018, **7**, 127–131.
67 IDK® Biotin ELISA, https://www.idkna.com/product/idk-biotin-elisa, (accessed November 20, 2025).
68 Biotin Quantitative Determination ELISA Kit - Elabscience®, https://www.elabscience.com/p/biotin-quantitative-determination-elisa-kit–e-ir-r501, (accessed November 20, 2025).
69 K. L. Singampalli, J. Li and P. B. Lillehoj, *Anal. Chim. Acta*, 2022, **1225**, 340246.
70 G. Schreiber, G. Haran and H.-X. Zhou, *Chem. Rev.*, 2009, **109**, 839–860.
71 A. A. Bhattacharya, S. Curry and N. P. Franks, *J. Biol. Chem.*, 2000, **275**, 38731–38738.
72 L. Trynda-Lemiesz and K. Wiglusz, *J. Pharm. Biomed. Anal.*, 2010, **52**, 300–304.
73 T. Peters Jr., *All About Albumin: Biochemistry, Genetics, and Medical Applications*, Academic Press, 1995. ISBN: 9780080527048.
74 L. Turell, R. Radi and B. Alvarez, *Free Radicals Biol. Med.*, 2013, **65**, 244–253.
75 B. T. Doumas, *Clin. Chem.*, 1975, **21**, 1159–1166.
76 M. Wilchek, *Protein Sci.*, 2004, **13**, 3066–3070.
77 T.-H. Xu, Y. Yan, K. G. Harikumar, L. J. Miller, K. Melcher and E. H. Xu, *Bio-Protoc.*, 2017, **7**, e2901.
78 S. Shan, Z. Zhong, W. Lai, Y. Xiong, X. Cui and D. Liu, *Food Control*, 2014, **45**, 138–142.
79 R. Vernet, E. Charrier, J. Grogg and N. Mach, *Vaccines*, 2021, **9**, 770.
80 C. Baine, J. Sembera, G. K. Oluka, J. S. Katende, V. Ankunda and J. Serwanga, *Bio-Protoc.*, 2023, **13**, e4905.
81 M. Hinsberger, J. Becker-Kettern, W. M. Jürgens-Wemheuer, J. Oertel and W. J. Schulz-Schaeffer, *Cancers*, 2023, **15**, 4096.
82 R. Xu, L. Ouyang, R. Shaik, G. Zhang and J. Zhe, *Sens. Actuator Rep.*, 2023, **5**, 100140.
83 R. Xu, L. Ouyang, R. Shaik, H. Chen, G. Zhang and J. Zhe, *Biosensors*, 2023, **13**, 721.
84 J. R. Lange, C. Metzner, S. Richter, W. Schneider, M. Spermann, T. Kolb, G. Whyte and B. Fabry, *Biophys. J.*, 2017, **112**, 1472–1480.